The following article appeared in Plasma Physics and Controlled Fusion, Vol.53, No.9, September 2011, p.095002
Multi-machine comparison of drift fluid dimensionless parameters
Militello F, Fundamenski W

Multi-machine comparison of drift fluid dimensionless parameters

F. Militello, W. Fundamenski

EURATOM/CCFE Fusion Association, Culham Science Centre, Abingdon, Oxon, OX14 3DB, UK

Abstract

The behaviour of the turbulence in magnetic fusion plasmas is discussed in the framework of dimensional analysis. Three main dimensionless parameters are identified, which directly affect the adiabatic response of the plasma and hence control the electron response. They were originally introduced by Scott [B. Scott, *Plasma Phys Control. Fusion*, **39**, 1635 (1997)] and Rogers and Drake [B.N. Rogers and J.F. Drake, *Phys. Rev. Lett.*, **79**, 229 (1997)], and represent the effect of the electromagnetic induction, collisions and electron inertia. The dimensionless parameters are then evaluated at different radial positions in four existing divertor machines (ALCATOR C-MOD, ASDEX-U, JET and MAST) and in three future experiments (MAST-U, ITER and DEMO). Clear multi-machine trends, suggesting a quasi-universal behaviour of the plasma, are identified and discussed. Exploiting this quasi-universality, useful insight in the physics of the machines is obtained without complex calculations or expensive numerical simulations. In particular, the trends show a clear separation of the plasma in four distinct regions: core, edge, Scrape-Off Layer and divertor, each of them characterized by a different set of parameters which, in turn, lead to significant variation of the dominant physical mechanisms across the machine.

I. INTRODUCTION

Plasma turbulence in tokamak generally determines the transport of particles, energy and momentum. Its understanding is therefore crucial to optimize the confinement and performance of a fusion reactor. However, the problem is complicated by at least two factors: (i) plasma turbulence involves multiple time and length scales; (ii) the background conditions in which it develops can change quite significantly, even within the vacuum vessel of the same machine, e.g. while in the plasma core temperature and density are high but their gradients are weak, in the plasma edge these conditions are reversed. As a consequence, analytical and numerical treatments need to face the challenge of coherently describing phenomena connected with each other, although separated by several orders of magnitude. In the presence of such complexity, it is useful to isolate and analyse the dominant dynamical processes that can alter the features of the turbulence and hence the magnitude of the radial transport and the quality of plasma confinement.

Dimensional analysis [1] is a powerful tool that can be employed to identify the key physical mechanisms governing complex systems. This technique has a long history of successful application in plasma physics, for example, Refs.[2, 3]. Ideally, experiments represented by the same set of dimensionless parameters behave in an identical way, as the plasma dynamics satisfies the same normalized equations. This implies that all the derived properties of the plasma, most notably the thermodynamic fluxes and forces, scale in a similar fashion and that their properly normalized versions depend exclusively on the dimensionless parameters. The wind tunnel approach made possible by these considerations is at the base of the scaling laws for energy and particle confinement time and provides a useful tool for designing future experimental devices (its limitations are discussed in Section III).

To avoid confusion, it is worthwhile to remark that the dimensionless parameters that we are discussing carry a specific dynamical meaning, in the sense that they represent the ratio between the characteristic weights of two physical mechanisms. In this respect, they are similar to the Reynolds number in fluid dynamics, which determines the relative importance between the inertial and viscous forces in Navier-Stokes equations. This clarification is useful because it helps to distinguish the dimensionless parameters from the numbers without units which are often encountered in physics in general, and in plasma physics in particular. These are not ratios of representative effects but only normalized quantities, such as the Greenwald

fraction, $f_{GW} = n/n_{GW}$, or the H-factor, $H_{98} = \tau_E/\tau_{E98}$.

Normally, in the study of physical phenomena, dimensionless parameters are obtained using one of these two methods (see [1]):

1. *Dimensional analysis*, which is a formal procedure that does not require to specify a physical/mathematical model (i.e. a set of equations) that describes the phenomenon, but only a set of variables that play a role in its determination (how these variables are chosen is left to physical intuition). In other words, the problem is cast in the form: $f(Q_1, Q_2, Q_3,) = 0$, where f is not determined and Q_i is the ith relevant dimensional variable. Buckingham Π theorem is then used to reduce the parameter space of the problem by normalizing the dimensional variables (which are typically more than the dimensionless variables). An application of this technique in plasma physics is given by Kadomtsev [2].

2. *Scale invariance*, which starts from a specific mathematical model and identifies its invariant transformations. These, in turn, provide constraints on how derived quantities (e.g. thermodynamic fluxes or confinement times) can vary within the given model, thus providing their relation to combinations of dimensional variables. These combinations can be cast in the form of the dimensionless parameters that we seek. This method was used by Connor and Taylor in [3].

Neither approach provides a unique set of dimensionless parameters, so that some degree of arbitrariness is still left. The standard set employed in plasma physics was suggested by Kadomtsev in his seminal paper [2]. The parameters that we discuss were obtained in the framework of drift-fluid models [4, 5] derived from Braginskii's equations [6] and are particularly well suited to characterize different turbulence regimes. Our approach can be seen as a mixture of both methods. Since most of them are a recombination of Kadomtsev's, our dimensionless parameters are model independent, but their choice is based on the physical insight provided by a specific set of equations, in this case the drift-fluid (and in particular Ohms law). This allowed us to identify some of the parameters with well defined physical effects, which lead us, for example, to recognize the importance of the balance between parallel and perpendicular physics (see Section II).

Using experimental density and temperature profiles for existing divertor machines (ALCATOR C-MOD, ASDEX Upgrade, JET and MAST), the dimensionless parameters are evaluated in different regions of the plasma, moving outwards from the core to the divertor. This analysis is repeated for future devices (ITER, DEMO and MAST Upgrade), based on

predicted density and temperature profiles. The chosen devices differ substantially in size, aspect ratio, magnetic field and heating power.

The paper is structured as follows. In Section II we introduce the model equations and derive the dimensionless parameters from first principles. In Section III, we describe the multi-machine trends of the dimensionless parameters and consider the limitations of the model employed. In Section IV we discuss the results, dividing the description of the physics on a 'geographical' basis, justified by the distinct separation of the dimensionless parameters in different regions of the plasma. In Section V, we draw our conclusions and we propose possible applications of our analysis. Appendix A provides a full derivation of the generalized Ohm's law, with the purpose of clarifying the physical meaning of the dimensionless parameters that we study. Finally, Appendix B examines the variability of the plasma engineering and dimensionless parameters in each machine in order to provide a rigorous statistical framework for our analysis.

II. DRIFT-FLUID DIMENSIONLESS PARAMETERS

The purpose of this Section is to define the dimensionless parameters we investigate and to clarify the physical effects they are associated with. A simple way to achieve this, is to briefly review the procedure that leads to the drift-fluid model from which they were originally derived [4, 5]. Following [4], we identify three main dimensionless parameters that naturally appear in the equations when a normalization relevant for drift-wave dynamics is introduced.

A. Physical Framework and Drift-ordered Ohm's Law

Cross-field transport in present-day fusion devices is dominated by drift-wave turbulence. The drift-waves are immersed in a strong confining magnetic filed, which produces a natural anisotropy and separates the dynamics in the parallel and perpendicular direction.

In particular, we expect the perpendicular dynamics to be slow (otherwise the confinement would not be good) in the sense that the characteristic velocity of the turbulent structures is much smaller than $c_s \equiv \sqrt{T_{e0}/m_i}$ (T_{sp0} and m_{sp} are the typical temperature and mass of the electrons, 'sp'='e', and ions, 'sp'='i'). Here, c_s can be interpreted as a measure of the plasma

sound speed (it is the cold ion sound speed or $2^{-1/2}$ times the isothermal sound speed). At the same time, due to their drift nature, we expect the fluctuations to be spatially localized on scales comparable to $\rho_s \equiv c_s/\Omega_i$, with $\Omega_i \equiv eB_0/(cm_i)$ the ion gyration frequency, c the speed of light, B_0 the characteristic amplitude of the confining magnetic field, and e the electron charge (singly charged ions are considered throughout the paper).

Conversely, the parallel dynamics are much faster because the particles are free streaming along the field lines. It is thus reasonable to assume that, on average, electrons and ions move at their thermal speed: $V_{th,e} \equiv \sqrt{T_{e0}/m_e}$ and $V_{th,i} \equiv \sqrt{T_{i0}/m_i}$, respectively. This, together with the continuity of the particle flux, implies that the turbulent eddies are elongated in the parallel direction [i.e. $L_\parallel \sim (V_\parallel/V_\perp)L_\perp$]. The typical parallel length scale of the perturbations is set by the ballooning structure of the modes and can be estimated as the connection length $L_\parallel \equiv qR \gg \rho_s$ (q and R are the safety factor and the major radius, respectively).

Finally, in the presence of a strong magnetic field, we expect the magnetization parameter, $\delta \equiv \rho_s/L_\perp \ll 1$, to be small. Here, $L_\perp \sim |\nabla \ln p_{eq}|^{-1}$ is the radial scale of variation of the equilibrium, which is typically of the order or smaller than the minor radius of the device, a. If also the collision frequency is small with respect to the gyrofrequency, $\nu_{sp}/\Omega_{sp} \ll 1$, the plasma is magnetized and the particles are strongly tied to the magnetic filed lines.

To summarize, the problems we focus on have a hierarchy of velocities: $V_\perp \ll c_s \sim V_{\parallel,i} \ll V_{\parallel,e}$, and of length scales: $L_\parallel \gg L_\perp \gg \rho_s$. If we limit our study to phenomena with these characteristics, the plasma model can be significantly simplified by employing a systematic procedure that allows to order the terms of the equations using the small parameter δ.

To make further progress, the perpendicular velocity can be estimated by introducing the drift ordering, which requires that $V_\perp \sim \delta c_s$. Since the perpendicular length scale is ρ_s, the typical time scale becomes the perpendicular transit time, $L_\perp/c_s$. The magnitude of the perpendicular electric field is implicitly dictated by the drift ordering. Indeed, by estimating the magnitude of the perpendicular velocity we are constraining the amplitude of the $\mathbf{E}\times\mathbf{B}$ drift, which obviously depends on $\mathbf{E}_\perp$. In particular, the perpendicular electric field must scale like $T_{e0}/(eL_\perp)$. At this point, an ordering is required also for the parallel velocity. For the sake of simplicity, several authors assume it to be comparable with the perpendicular velocity, so that also the parallel velocity scales like δc_s. Although this choice greatly simplifies the equations, it is not strictly relevant, since, as discussed before, a more

realistic estimate sets the value of the parallel velocity of the two species at their respective thermal speed. A better assumption is that $V_{\parallel,i} \sim c_s$ and $V_{\parallel,e} \sim (m_e/m_i)^{-1/2} c_s$, where $\sqrt{m_e/m_i} \simeq 0.024$ is another small parameter that can be used to simplify the equations.

The result of this systematic procedure is a set of equations, which can be conveniently normalized with time and length scales typical of the drift-ordered dynamics. In particular, it is useful to write down the parallel momentum conservation for the electrons, i.e. the generalized Ohm's law [4] (see Appendix A for a complete discussion, including the definition of the variables):

$$\widehat{\beta}\frac{\partial A_\parallel}{\partial t} + \widehat{\mu}\left(\frac{\partial}{\partial t} + \mathbf{V}_E \cdot \nabla\right) J_\parallel = \nabla_\parallel (p_e - \phi) - C J_\parallel + 0.71 \nabla_\parallel T_e + S^{(4)}_{eq}, \tag{1}$$

B. Dimensionless Parameters

The drift-fluid models can provide useful insight in the nature of the turbulence and therefore on the properties of the transport. In this regard, the three dimensionless parameters appearing in Eq.1 and listed below are particularly significant:

$$\widehat{\beta} = \beta \left(\frac{L_\parallel}{L_\perp}\right)^2 \tag{2}$$

$$\widehat{\mu} = \frac{m_e}{m_i}\left(\frac{L_\parallel}{L_\perp}\right)^2 \tag{3}$$

$$C = 0.51 \nu_* \left(\frac{m_e}{m_i}\right)^{1/2} \left(\frac{L_\parallel}{L_\perp}\right), \tag{4}$$

where $\nu_* = \nu_e L_\parallel / V_{th,e}$ is the electron collisionality (in absence of banana orbits). These parameters are related to Kadomtsev's [2] through the factor $L_\parallel/L_\perp$, which weighs the relative importance of the parallel and perpendicular dynamics. They represent the importance of the electromagnetic part of the electric field, the electron inertia and the effect of the collisions, respectively. All the parameters directly affect the generalized Ohm's law, Eq.1, and thus determine the parallel electron response. The values of $\widehat{\beta}$, $\widehat{\mu}$ and C are therefore crucial, as they determine the departure from adiabaticity of the plasma regime and set the phase relation between the fluctuating density, temperature and electric potential, which, in turn, regulate the properties of the transport.

III. MULTI-MACHINE TRENDS

In this Section, the dimensionless parameters are employed to characterize the plasma regimes, which are reviewed in different regions of various experimental machines. As a practical application, it would be desirable to correlate $\widehat{\beta}$, $\widehat{\mu}$ and C to the normalized cross-field particle and energy fluxes in the closed field line region, and to the divertor and wall fluxes in the open field line region. By expressing these fluxes in terms of these three dimensionless parameters, i.e. by writing the normalized effective transport velocity $[V_{\perp,eff} \sim (\Gamma/n, q/p)]$ as

$$\frac{V_{\perp,eff}}{\delta c_s} = \widehat{V}_{\perp,eff}\left(\widehat{\beta}, \widehat{\mu}, C, \dots\right), \tag{5}$$

one could predict their value in larger (or future) devices based on the direct measurements in smaller ones. This *wind tunnel* approach, as it is generally known, relies on the ability to match the dominant dimensionless parameters while changing the systems size. Hence, classical wind tunnel experiments are useful because in *incompressible* hydrodynamics, the aerodynamic forces (drag and lift) are determined (mainly) by the Reynolds number, i.e.,

$$C_D \equiv \frac{F_D}{\rho V_\infty^2 A} = \widehat{F}_D(Re), \qquad Re = V_\infty L/\nu, \tag{6}$$

where ρ, V_∞ and A are the characteristic density, velocity and relevant surface of the fluid. Assuming ν is a property of the fluid, two systems of different sizes are thus *dynamically similar* (have same Re) provided that their inflow velocities scale inversely with their size ($V_\infty L = const$).

Such a dimensionless similarity approach is effective if, and only if, the dominant physical mechanisms are properly captured by the chosen dimensionless parameters and these parameters can be kept constant while changing the system size! When either of these conditions is not met, a similarity experiment is not possible. A good example is the case of *compressible* hydrodynamics (i.e. when flow velocities are comparable to the sound speed, C_S), which differs from the incompressible case by the appearance of compressional dissipation, most notably shock waves, hence an additional drag force, generally known as *wave drag* (This means that compressible flow is qualitatively different from the incompressible case, being governed by hyperbolic and parabolic equations, respectively). The strength of these compressional forces is measured by an additional dimensionless parameter, the Mach

number, M, and the wave drag can be written as,

$$C_W \equiv \frac{F_W}{\rho V_\infty^2 A} = \widehat{F}_W(M), \qquad M \equiv V_\infty / C_S. \tag{7}$$

Assuming ν and C_s are properties of the fluid, two systems are *dynamically similar* (have same Re and M) if and only if they have the same inflow velocity and size, thus preventing an effective similarity experiments (this explains why wind tunnel experiments are common for aircraft design but not in ship design). As we will see in section E, an analogous situation occurs in fusion plasmas with either significant amount of fusion reactions (burning plasmas) or strong interactions with neutrals (divertor and SOL plasmas), which introduce additional dimensionless parameters and preclude proper similarity experiments.

In the first part of this Section, we describe the trends of the dimensionless parameters in both the H- and L-mode of the machines examined. Together with the data, we provide a brief discussion of the regimes they represent. We then touch a few arguments that are tangential to the main discussion, but that are needed to complete the physical description required by our analysis. Firstly, we consider the magnetic configuration in the edge and SOL regions of the plasma and its impact on the transport. Then, we investigate the effect of plasma-neutral interaction and fusion reactions on our study. Finally, we comment on the possibility that the magnetization of the plasma could become weaker under certain conditions.

A. Multi-machine dimensional quantities

We begin by presenting the geometrical features and the characteristic value of the confining field of the devices studied, which are summarized in Table I. For each machine, we identify *typical* electron temperature and density profile in six different radial positions, which, as emerges from our analysis, correspond to regions of distinctive plasma behaviour. In particular, the data analysed are localized in the core (on the magnetic axis), in the edge, which lies between the pedestal top (at 95% of the minor radius) and separatrix, in the SOL, where we identify a near SOL (ending at 101% of the minor radius) and a far SOL (ending at 105% of the minor radius), and finally at the divertor plate (assuming a detached divertor regime).

Of course, due to the variability of the plasma conditions in different pulses of the same

TABLE I. Confining magnetic field and geometry of the experimental devices.

	B_0 (Tesla)	R_0 (cm)	ϵ
ALCATOR C-MOD	5.3	67	0.33
ASDEX U.	2.5	165	0.36
JET	2.5	296	0.33
ITER	5.3	620	0.33
DEMO	7.0	950	0.33
MAST	0.5	85	0.70

device, the values in our tables have to be considered as order of magnitude estimates rather than exact measurement/predictions. To be more precise, where possible, the numbers shown were obtained through a statistical analysis of the ITPA databases (Pedestal, Profiles, H-mode and L-mode) [21, 22]. The *typical* values for a certain machine are then the averages over the pulses in the same regime (e.g. Ohmic L-mode or H-mode with small ELMs). This also allowed us to estimate the machine variability, associated to the standard deviation of the data analysed. In general, for a given radial position, we found that the variability of a measured quantity in the same device is smaller than the change that occurs passing from one machine to another. This implies that the *typical* values of temperature and density are indeed characteristic of the machine studied in a certain regime (H- or L-mode) and at a given radial position. The details of the procedure used to obtain the average values as well as an estimate of the variability are discussed in Appendix B. Unfortunately, a statistical analysis was not possible in the following two cases: i) for data beyond the separatrix (not given in the ITPA database), ii) for machines yet to be built. In the first case, we relied on referenced published measurements, while in the second we used predictions or extrapolations from theoretical or numerical models (see discussion below).

With this in mind, plasma profiles are given in Tables IV and V for L-mode, and in Tables II and III for H-mode. The L-mode values do not include the pedestal top and are limited to the active machines. Finally, note that the divertor region in detached conditions is characterized by a rather universal temperature, which is given by atomic processes (the balance between charge exchange and ionization cross sections sets the divertor temperature around $5eV$ for Deuterium) [24], while the density value is particularly high and assumed

comparable to the pedestal top.

The reliability of the *typical* values obtained through the statistical analysis of the ITPA databases was further verified by comparing them with more recent data extracted form the experimental works listed below (which were the source of our SOL values). For each machine, we also state the plasma regime examined.

ALCATOR C-MOD: the profiles are representative of L-mode and ELM-free H-modes [11, 12].

MAST: typical Sawtooth-free L and H modes were considered [13–15]. The profile measurement in the edge-SOL are complemented with B2-SOLPS predictions. In our analysis, we have also included the MAST device in its Super-X Divertor (SXD) configuration, which will be implemented in the framework of the MAST-Upgrade project. The principal feature of the SXD is the increase of the connection length in the open field line region, which will be two or three times longer than in the present MAST. This is obtained by a modification of the confining magnetic field and by moving the outer divertor plate to a larger major radius. The SXD is beneficial in many ways since it reduces the heat fluxes by increasing the wetted area, and it reduces the target temperature as a consequence of the longer connection length. In our study, we have simulated this configuration by increasing $L_{\|}$ by a factor 3 in the outer region of the plasma (from the separatrix outward), while keeping the same temperature and density profile of the present MAST device. Of course, this is not a completely self-consistent treatment, since the new divertor is expected to affect the profiles. As a consequence, the MAST SXD data have to be considered as a first order approximation.

ASDEX: we considered a typical L-mode and ELMy H-mode plasmas [14, 16–18] and used, where possible, Thomson scattering measurement integrated with B2-SOLPS simulations.

JET: we considered typical L-mode and ELMy H-mode discharges, supplemented by EDGE2D/EIRENE simulations [19, 20].

ITER and DEMO: for the future experiments, we have based our study on the most reliable simulations and theoretical predictions available in literature ([21, 23] for ITER and the final report of the European fusion power plant conceptual study for DEMO). In these machines, we modelled the open field lines region by rescaling JET's experimental profiles or, when the estimated divertor loads were given, by using the two point model [24].

TABLE II. Electron temperature (in KeV) in the six regions of the machines investigated (H-mode). The variability of these data is given in Appendix B.

		Edge		SOL		Detached
	Core	Pedestal Top	Separatrix	Near SOL	Far SOL	Divertor
ALCATOR C-MOD	3	0.4	0.1	0.02	0.01	0.001
ASDEX U.	2.8	0.45	0.09	0.03	0.01	0.001
JET	3.6	1	0.12	0.04	0.03	0.001
ITER	20	5.3	0.2	0.05	0.04	0.001
DEMO	50	5	0.16	0.04	0.03	0.001
MAST	1.3	0.1	0.06	0.015	0.01	0.001

TABLE III. Plasma density (in $10^{19}m^{-3}$) in the six regions of the machines investigated (H-mode). The variability of these data is given in Appendix B.

		Edge		SOL		Detached
	Core	Pedestal Top	Separatrix	Near SOL	Far SOL	Divertor
ALCATOR C-MOD	29	20	1.75	2	1	20
ASDEX U.	8.5	5	2.5	0.8	0.3	5
JET	7.5	4.85	2.25	1.1	0.4	7
ITER	12	7	5	1.6	0.6	7
DEMO	14	9	4.5	1.4	0.5	9
MAST	3.8	4.2	0.5	0.45	0.3	4

TABLE IV. Electron temperature (in KeV) in the five regions of the machines investigated (L-mode). The variability of these data is given in Appendix B.

			SOL		Detached
	Core	Separatrix	Near SOL	Far SOL	Divertor
ALCATOR C-MOD	1.9	0.095	0.045	0.02	0.001
ASDEX U.	1.3	0.085	0.04	0.01	0.001
JET	3.2	0.075	0.03	0.01	0.001
MAST	1.1	0.05	0.035	0.01	0.001

TABLE V. Plasma density (in $10^{19}m^{-3}$) in the six regions of the machines investigated (L-mode). The variability of these data is given in Appendix B.

			SOL		Detached
	Core	Separatrix	Near SOL	Far SOL	Divertor
ALCATOR C-MOD	17	11	5	1	10
ASDEX U.	7	2	1	0.3	2
JET	3.7	1.2	0.7	0.1	2
MAST	5	0.8	0.5	0.1	1

Inevitably, several machines of interest do not appear in our list. However, some of them present similarities to the devices that we analysed. Thus, JT-60U and NSTX can be represented by the entries of JET and MAST, while DIII-D and KSTAR are comparable to ASDEX U. Finally, the size and the large magnetic field in ALCATOR C-MOD make it compatible with FTU, although the latter is a limiter machine.

The tables I to V allow us to estimate β, c_s, ν_e. Whenever the equilibrium length scale, $L_\perp$, is not provided in our references, it is evaluated using the temperature and density profiles. In addition, we assume that its core values does not change from L-mode to H-mode because of stiffness and that the in L-mode the edge value is approximatively one tenth of the core's. The H-mode values of $L_\perp/a$ are shown in Fig.1. The parallel connection length, $L_\parallel$ can be determined from the profile of the safety factor, which we assume common to all the machines. In particular, we take $q = 1$ in the core, $q = 3$ at the pedestal top and in the far SOL, $q = 5$ in the near SOL and $q = 10$ at the separatrix. The latter assumption is motivated by the saturation of the safety factor profile due to the stochastization of the layer between the last closed field surface and ideal separatrix [25]. The connection length at the divertor plate is calculated assuming that it is one tenth of the major radius. Once all these quantities are estimated, the dimensionless parameters are straightforwardly obtained.

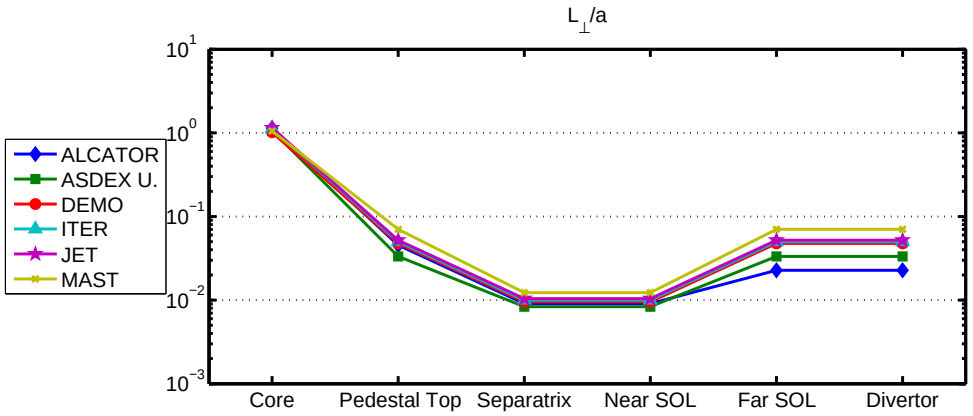

FIG. 1. The ratio $L_\perp/a$ in the six characteristic regions of each machine (H-mode).

B. Multi-machine dimensionless analysis: H-mode

We start the discussion of our data with the H-mode case. In Fig.2, we plot $\widehat{\beta}$ in the six regions. A common feature of all the machines is the smallness of this parameter in the core and in the far SOL (with the exception of MAST SXD), while the edge region always appears to be strongly electromagnetic (i.e. $\widehat{\beta} \gg 1$). Although our analysis shows a clear and dominant cross-machine trend, we can still identify weaker tendencies. Thus, larger machines (i.e. larger R) appear to be more electromagnetic in the core than smaller ones, while the opposite happens in the SOL. For similar size machines, such as MAST and ALCATOR C-MOD, the different confining magnetic field and aspect ratio play a significant role in the edge region (including the near SOL), but only produce a moderate change in the core and in the far SOL. Only MAST-U stands out from the common trend (from the separatrix outward), suggesting that an unconventionally long divertor leg could strongly affect the electromagnetic properties of the machine's edge and potentially lead to unexplored dynamical regimes.

Figure 3 describes the importance of the electron inertia term, proportional to $\widehat{\mu}$. This effect is largely negligible in the core of the plasma, while it is significant in the edge and SOL regions and again small at the divertor plates with the possible exception of MAST SXD and ALCATOR. $\widehat{\mu}$ can also be interpreted as a measure of the self-similarity of the plasma pressure profiles since $L_\perp$ is the radial pressure gradient length. The MAST data appear shifted downward consistently, as a consequence of the larger aspect ratio (i.e. the gradients are self-similar when scaled with respect to the minor radius but they are not

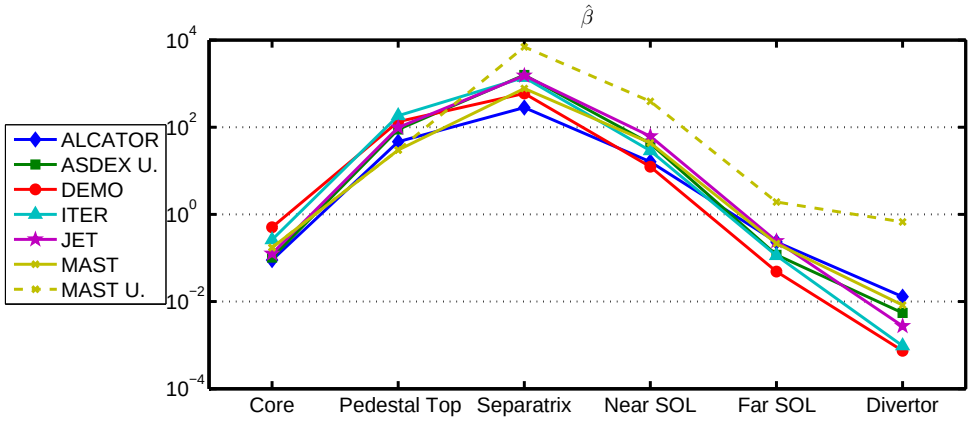

FIG. 2. The dimensionless parameter $\widehat{\beta}$ in the six characteristic regions of each machine (H-mode).

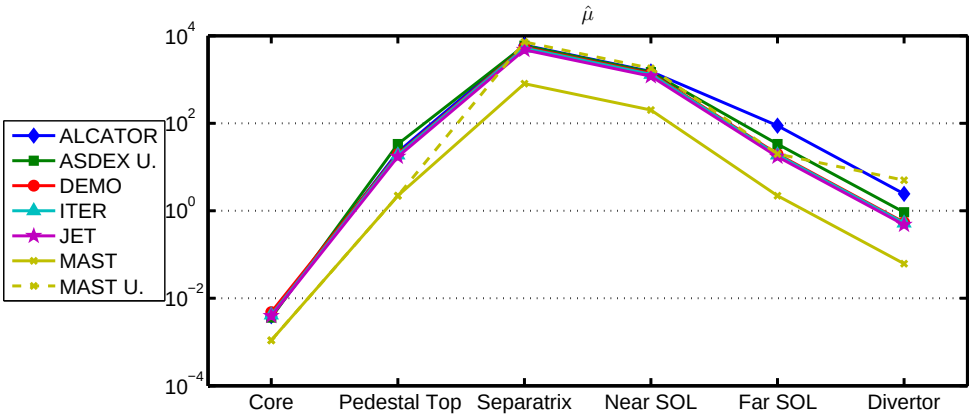

FIG. 3. The dimensionless parameter $\widehat{\mu}$ in the six characteristic regions of each machine (H-mode).

when they are scaled with respect to R).

Finally, the behaviour of the collisional parameter, C, is depicted in Fig.4. This parameter has the largest variation among the three, with values increasing from 10^{-6} in the core to 10^4 in the divertor region, while the clustering of the profiles is the least marked. It also exhibits a size dependence, which is inverse with respect to $\widehat{\beta}$ (i.e. larger machines are less collisional in the core) and even more marked. This similarity is reinforced by the fact that the trend reverses passing from the core to the edge. It is interesting to note that ALCATOR C-MOD does not follow these size trends, which could be related to its large magnetic field with respect to its size.

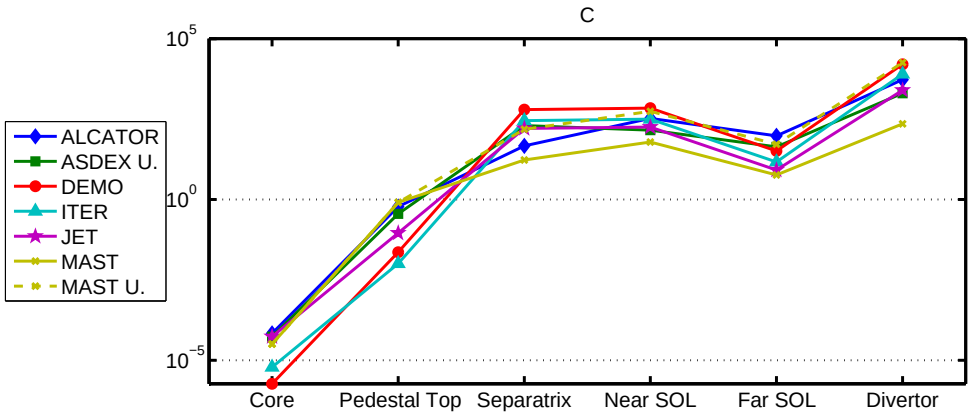

FIG. 4. The dimensionless parameter C in the six characteristic regions of each machine (H-mode).

C. Multi-machine dimensionless analysis: L-mode

We move now to the L-mode profiles. The most important difference with respect to the H-mode case is the significant increase of the perpendicular equilibrium length scale in the edge region of the plasma (i.e. the pedestal is not present and the gradients are less steep). This directly affects the dimensionless parameters, which depend quadratically ($\widehat{\beta}$ and $\widehat{\mu}$) or linearly (C) on the inverse of $L_\perp$. As a consequence, all the non-adiabatic effects are much weaker in the L-mode than in the H-mode, as Figs.5-7 show.

Apart from the absolute values, the curves drawn by the parameters have the same shape of those in H-mode. In particular, in L-mode, the values are typically similar or slightly smaller than in H-mode everywhere in the plasma, with the exception of the pedestal region, where the difference is more marked (it can reach three order of magnitude). It is also interesting to note that, apart from MAST (and JET in the case of $\widehat{\beta}$), the data are much less scattered than in the H-mode, which would suggest a difference in the L-mode between tokamak and spheromaks.

D. Equilibrium and magnetic configuration

In most theoretical models the existence of a well defined plasma equilibrium (or at least of a quasi steady-state configuration) is implicitly assumed. In order to yield acceptable energy and particle confinement, this equilibrium has to be stable with respect to large scale MHD perturbations although it is often difficult to ensure at the same time its stability with

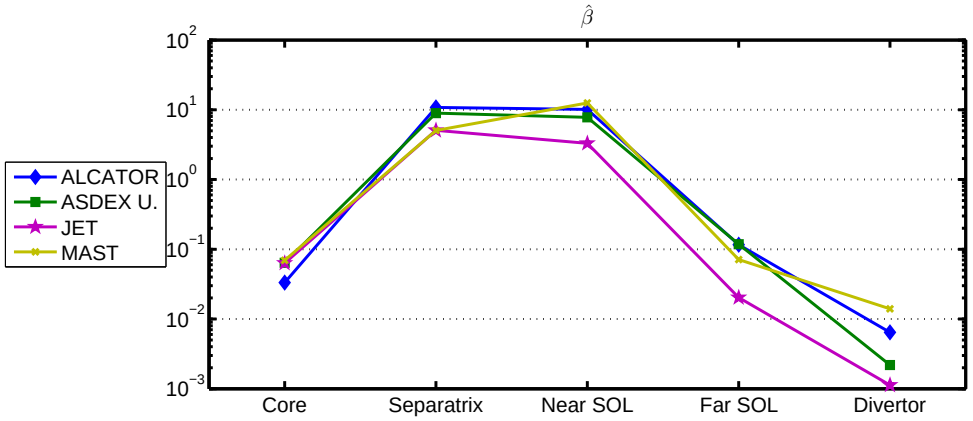

FIG. 5. The dimensionless parameter $\widehat{\beta}$ in the five characteristic regions of each machine (L-mode).

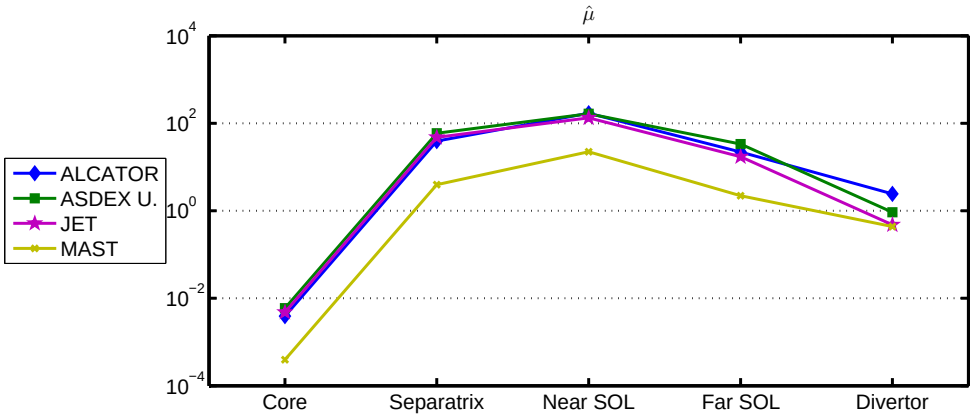

FIG. 6. The dimensionless parameter $\widehat{\mu}$ in the five characteristic regions of each machine (L-mode).

respect to transport driving micro-instabilities. Furthermore, the magnetic configuration which confines the plasma should maintain its coherence on a longer time scale with respect to the other relevant plasma phenomena (reconnection instabilities are therefore deleterious in this respect). In other words, the current profile should adapt more slowly to source changes than the density or temperature profile.

This is the case if the diffusion of the magnetic field in the plasma is less efficient than the particle/energy diffusion. While both phenomena are highly complex, we can simplify the discussion by assuming that the former is mainly due to resistive effects, so that $D_\eta = \eta/\mu_0$ where η is the resistivity and μ_0 is the vacuum permeability, and that the latter can be measured by the Neoclassical, Bohm or Gyro-Bohm values. The Neoclassical diffusivity is due to collisional processes in toroidal geometry, and as a consequence is relevant only when turbulence is quenched, i.e. in the transport barrier. The Bohm and Gyro-Bohm diffusivity

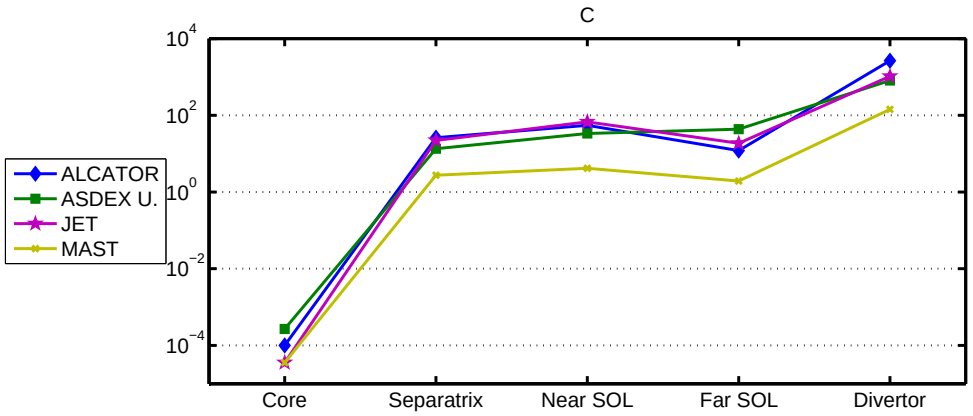

FIG. 7. The dimensionless parameter C in the five characteristic regions of each machine (L-mode).

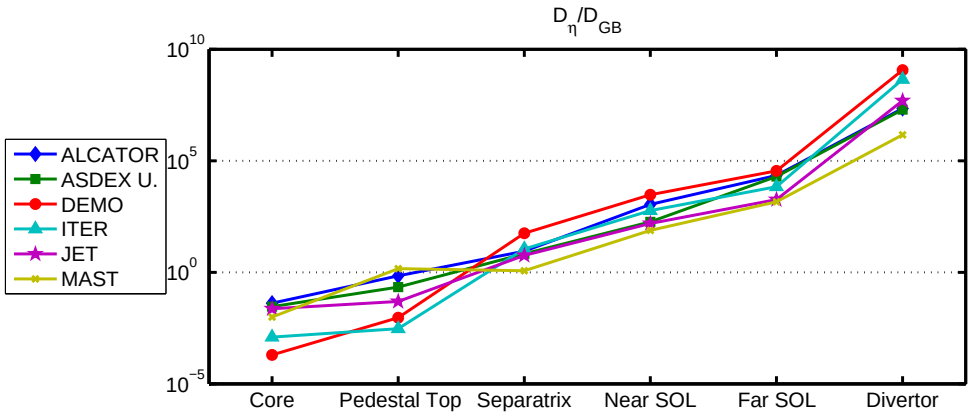

FIG. 8. Ratio between the magnetic and the Gyro-Bohm diffusivity in the six characteristic regions of each machine (H-mode).

are mixing length estimates in which the fluctuations are assumed to be machine size and non-local or microscopic and of drift wave nature, respectively.

The figure of merit for the existence of a good magnetic configuration is the ratio between the magnetic and particle diffusivity, $d = D_\eta/D$, where D can be the Neoclassical, Bohm or Gyro-Bohm value. If d is larger than one, the loss of confinement is mainly due to the variation of the magnetic field rather than to the plasma micro-instabilities.

In our analysis of the H-mode data, we assume that $D = \delta\rho_s c_s$ (Gyro-Bohm). Figure 8 shows d in the six regions of the machines. In the pedestal region (i.e. at the pedestal top, separatrix and near SOL), the diffusion should be reduced to Neoclassical levels and d should be larger than the one reported. In any case, it appears that the magnetic field coherence deteriorates from the Edge Transport Barrier outward, yet another evidence of

the complexity of the plasma edge. In other words, the frozen-in condition is not valid in the outer region of the plasma, so that the fluid elements are free to slide through the magnetic field without impediment. This also implies that the separatrix region and the SOL are not in a proper MHD equilibrium.

E. Neutrals and burning plasma

Two important elements are so far excluded from our analysis. These are the interaction between the plasma and the neutrals (i.e. ionization and recombination) and the effect of fusion reactions. The former is relevant in the cold regions of the plasma (or in the presence of Neutral Beam Heating) and plays an important role in the SOL and divertor region, while the latter only acts in the hot core of the largest devices. A common feature of these atomic and nuclear processes is that they both depend on cross-sections, which are a function of the temperature of the plasma. The introduction of these physical mechanisms in our equations would lead to the loss of a scaling invariance [3], which implies that a new dimensionless parameter is introduced in the problem (recall the discussion at the beginning of Section III). This dimensionless parameter must be the same for two plasmas to be similar in terms of atomic and nuclear reactions. This new constraint is severe and can be satisfied in a non-trivial way only if another similarity condition is dropped. In other words, in the presence of fusion reactions or strong neutral interactions, in order to have two equivalent plasmas that are not the same plasma, we must either assume that the plasma is electrostatic or that the collisionality level is not important (the effect of the Larmor radius should be retained, as it is essential to the transport mechanisms).

In the context of dimensionless analysis, this problem was discussed in Ref.[27] for the interactions with the neutrals and in Ref.[28] for burning plasmas. A direct consequence on our study is that, despite the universal behaviour observed in Figs.2-7, the machines discussed might still present significant differences due to presence of neutrals or fusion effects. Clearly, ITER and DEMO will have a significant alpha particle heating in the core, which will set them apart from each other and from the present-day machines (which are, instead, comparable). Regarding the edge, SOL and divertor regions, Lackner [27] suggested that the similarity with respect to neutral interactions (for binary collisions) must rely on the identity of the absolute value of the temperature, as this implies comparable cross-sections.

In low-β plasmas this leads to a relevant figure of merit given by P/R, where P is the total power crossing the separatrix. Using this approach, present-day machines would not be representative of ITER and DEMO, which are characterized by a much larger value of P/R. On the other hand, experimental scalings of the SOL width [29] seem to suggest that that the appropriate figure of merit for the SOL similarity is P/R^2 rather than P/R, which would allow extrapolations of the present-day experiments to future machines. In the context of this dispute, we remark that Lackner's approach requires that the electromagnetic effects are negligible, which is a good approximation in the far SOL and close to the divertor, but does not hold in the edge region (see Fig.2 and 5). In addition, the similarity criterion based on P/R is based on the assumption that the divertor is in a conduction limited regime. Therefore, neither the sheath limited regime nor, most importantly, the detached divertor regime are properly described by it.

It is useful, at this point, to evaluate P/R^2 (and for completeness also P/R) for the machines we are considering. Before doing that we need to find a proxy for the power crossing the separatrix, which cannot be directly measured. We consider two options, the first is $P = P_{heat}$, where P_{heat} is the total heating power (auxiliary plus alpha heating) and the second is $P = P_{L-H}$, where P_{L-H} is the L-H transition power threshold. The former was adopted in Ref.[29], where the value of P_{heat}/R and P_{heat}/R^2 for ALCATOR, ASDEX-U, JET and ITER can be found. The picture is completed by the MAST and DEMO numbers, which we calculate in table VI. While the simplicity of this choice makes it attractive, it might not be the most appropriate, as a consequence of the fact that it does not take into account the possible differences in the radiative losses in the different machines. To this effect, the L-H transition power is a more representative quantity. For the large aspect ratio machines we have calculated P_{L-H} using the Martin scaling [30], while for MAST and MAST-Upgrade we have used the scaling of Ref.[25] which better represents spherical tokamaks (the density used is the average between the core and the pedestal top). Incidentally, it is interesting to note that most of the machines have a large excess of power available, so that the P_{heat}/P_{L-H} ranges between 2 and 4. However, ITER will operate with significantly less margin, although the L-H transitions should still be easily achieved at low density.

Despite the different definitions of P, our results do not differ much in the two cases. It is interesting to note that, using P/R as the similarity parameter, the present-day tokamaks

TABLE VI. Typical heating power (including fusion power), L-H threshold power and divertor similarity parameters for the machines examined. The power is expressed in MW, while the major radius is expressed in meters.

	P_{heat}	P_{L-H}	P_{heat}/R	P_{heat}/R^2	P_{L-H}/R	P_{L-H}/R^2
ALCATOR C-MOD	6	2.2	9	13.4	3.3	4.9
ASDEX U.	14.5	3.8	8.8	5.2	2.3	1.4
JET	25.2	10.3	8.5	2.9	3.5	1.2
ITER	130	94.1	21	3.4	15.2	2.5
DEMO	1490	327	157	16.5	34.5	3.6
MAST	3	1	3.5	4.1	1.2	1.4
MAST-U	7.5	2	8.8	10.3	2.3	2.7

considered would be similar, although, as already noted by Lackner, far from the ITER and DEMO divertor regime. At the same time, MAST appears to be in a different category, although the new installed power introduced with the Upgrade should align the machine with the others (here the Super-X divertor may affect the divertor operations). On the other hand, the disparate values of P/R^2 suggest that the the divertors of the machines we have examined are likely to operate with a different underlying physics (i.e. the divertors are at most moderately similar). In this respect, ALCATOR C-MOD and MAST-U should be comparable and used for DEMO extrapolations, while JET would be in the same regime as ITER.

Finally, it is worth mentioning that another parameter often related to the presence of the neutrals is the Greenwald fraction [31], which represents the proximity of the plasma to the disruptive density limit. It is given by the ratio between the plasma line averaged density and the Greenwald density, $n_{GW} \equiv I_p/(\pi a^2)$, where I_p is the plasma current. The physical mechanism associated with this parameter is not completely clear, but the experimental observations indicate edge cooling and energy confinement degradation when it reaches values of order unity, ultimately loss of the H-mode, MARFE formation at the X-point and termination of the discharge (radiative collapse). The cooling is likely to be caused by an increased cross-field transport and/or by radiation losses (related to neutral-plasma interactions). Despite its connection with neutral physics, the Greenwald fraction is not a good

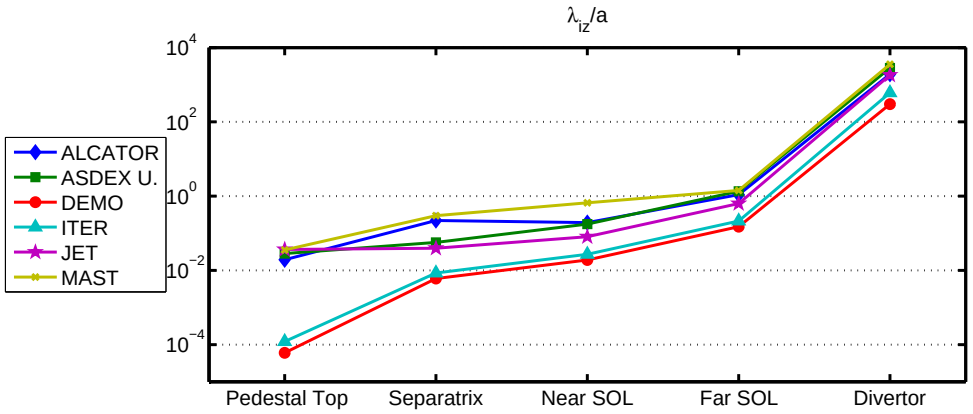

FIG. 9. Ratio between between the neutral penetration distance in the plasma and the minor radius of the machine in the six characteristic regions of each machine (H-mode).

scaling factor, as noted in Ref.[21], for the confinement time. We therefore do not include it in our main dimensionless parameters. The same argument applies to the normalized energy confinement time, H_{98}.

F. Penetration of the neutral particles

To further assess the relative importance of the neutral particles, it is useful to introduce another dimensionless parameter in the form of the ratio between the penetration distance of the neutrals in the plasma and the minor radius of the machine. The former measures how deep a particle can travel through the plasma before getting ionized and is defined as $\lambda_{iz} = v_n/[n_e\overline{\sigma v_{iz}}(T_e)]$, where v_n is the velocity of the neutrals and $\overline{\sigma v_{iz}}(T_e)$ is the ionization rate coefficient. For our analysis, we take Franck-Condon atoms, which are produced by an electron impact with an hydrogen molecule. This process takes the atoms above their thermal velocity, giving them a roughly constant kinetic energy of about 3 eV [24] (from which we deduce $v_n \approx 1.7 \cdot 10^4$ m/sec). The value of the electron impact ionization rate of hydrogen atoms can be found tabulated in literature [24], so that λ_{iz} is well defined.

Figure 9 shows the trend of λ_{iz}/a across the boundary of the plasma (the core is excluded from this plot as it is of modest interest). It is interesting to note that also this parameter shows a clustering of the data for the present-day machines, although it appears that the future devices will have a different behaviour. As a consequence, the physics involved in the external fuelling mechanisms in ITER and DEMO might differ from the one studied in the

available experiments. In particular, the gas puff fuelling might not be efficient in the future devices, since the penetration of the neutrals is quite shallow already in the Far SOL.

G. Plasma magnetization

We complete this Section by verifying the validity of one of the main working assumptions used in the derivation of several plasma models. Fluid equations, such as Braginskii's, are moments of Boltzmann equation, asymptotically closed through a perturbative technique which relies on the smallness of an expansion parameter. This procedure allows to find an approximate solution of the kinetic equation, the leading order of which is locally almost Maxwellian. In the standard treatment of a collisional plasma, this solution is valid only as long as the typical length scale of the phenomena that we study is longer than the mean free path of the particles, λ, and the time scale is slower than the collisional time, ν^{-1}. In other words, $L_\parallel, \rho_s \gg \lambda$ and $(c_s/L_\perp)^{-1} \gg \nu^{-1}$. At the same time, Braginskii's transport coefficient are obtained for plasmas in which the particles motions are dominated by the magnetic field, $\nu_i/\Omega_i \ll 1$ and $\nu_e/\Omega_e \ll 1$ ($\nu_{e,i}$ are the electron and ion collision frequencies and Ω_e is the electron gyrofrequency). This condition sets an upper limit to the collisionality.

In modern experimental devices the mean free path is comparable or larger than the scale of interest, requiring a different approach to the closure problem. In the direction perpendicular to the magnetic field, the closure can be obtained assuming that the plasma is magnetized, which ensures a certain coherence of the fluid elements and therefore enables a local treatment. On the other hand, along the magnetic field the particles are free streaming and a different closure, necessarily dependent on the magnetic field geometry, is required. In this regard, systems with small δ *and* closed magnetic field surfaces, like the region inside the separatrix of magnetic fusion devices, remain suitable for analytic treatment since their distribution function is approximately Maxwellian regardless the collisionality (see e.g. [7, 8]).

The parameter δ, and in particular the assumption that it is small, therefore plays a special role in the construction of plasma models. As Fig.10 shows, in H-mode this condition is met everywhere in the large machines, while it breaks down in the edge region of ALCATOR and especially of MAST. As a consequence, in the small machines the edge physics is further complicated by the fact that the plasma is weakly magnetized, with the particles loosely

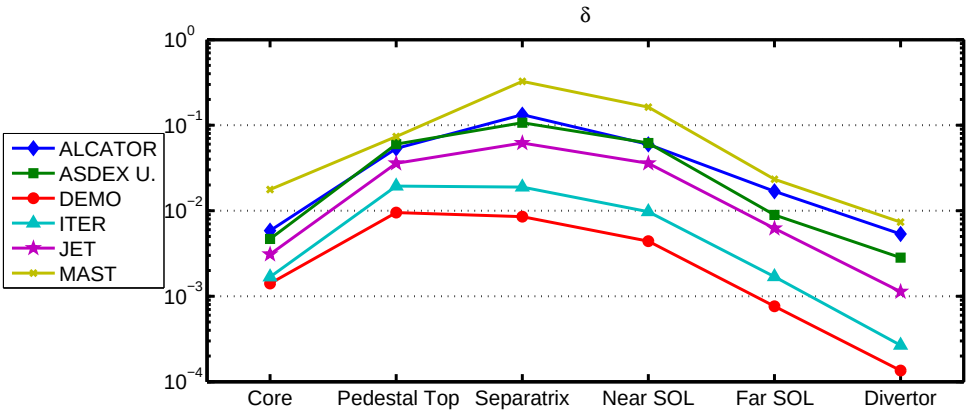

FIG. 10. The magnetization parameter δ in the six characteristic regions of each machine (H-mode).

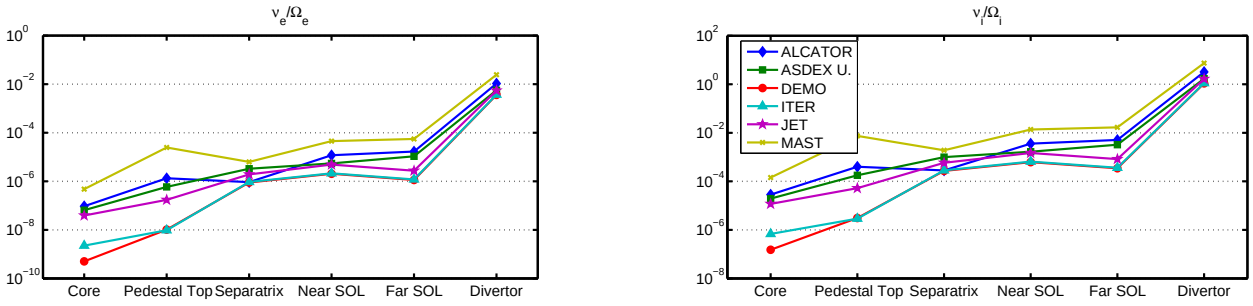

FIG. 11. The ratios ν_e/Ω_e and ν_i/Ω_i in the six characteristic regions of each machine (H-mode).

tied to the magnetic filed lines. In these conditions, the fluid models lose validity and even the gyrokinetic drift approximation no longer accurate.

Another important assumption used in the model is the smallness of the factors ν_i/Ω_i and ν_e/Ω_e, from which we could approximate the transport coefficients to Braginskii's. Figure 11 shows that this is a reasonable approximations everywhere in the plasma except from the region surrounding the detached divertor plates, where the ions are highly collisional. On the other hand, we remark that even in the relatively cold SOL, the Braginskii's equations are never rigorously valid since the second condition on the collisionality, $\nu_e/(c_s/L_\perp) \gg 1$, is never achieved.

IV. DISCUSSION

The results in the previous section show a remarkable variety of physical regimes as we move outwards from the center of the machine towards the periphery. Each of them

has peculiar features which deserve a more detailed discussion. We give here a coherent description of the phenomena occurring in the different regions of the plasma by linking them to the appropriate dimensionless parameters. When possible, we organise our conclusions by touching the important topics of equilibrium (i.e. stochastic layer), (in)stability (i.e. ELMs), and transport/turbulence (i.e. L-H transition, density limit). Finally, we discuss how some of our results can be used in the perspective of giving an integrated description of the plasma.

A. Core

We start with the core, which is characterized by the smallness of all the dimensionless parameters. Indeed, the collisionality is very weak and constantly decreasing in the most powerful machines, as a consequence of its inverse proportionality with the temperature. This entails the possibility of stronger inward density pinch in the future devices, which would lead to both favourable (higher fusion gain) and unfavourable (NTM destabilization and impurity accumulation) effects. Also the electron inertia is negligible and does not directly affect the transport. However, despite its smallness, it can break the plasma frozen in condition and allow for collisionless magnetic reconnection, which manifests in the form of tearing modes and sawtooth oscillations [32, 33]. Finally, the magnetic induction is fairly small but increasing with the machine size, which suggests that in reactor conditions electromagnetic effects could affect the turbulence behaviour even in the core.

It is also interesting to note that the value of $\widehat{\beta}$ is slightly larger for MAST than for most of the other active machines. This appears to be consistent with the common assumption that turbulence is more electromagnetic in low aspect ratio devices. Spherical tokamaks usually operate at high β. However, the figure of merit for the electromagneticity of the turbulence is $\widehat{\beta}$, which also includes a weight of the relative importance of parallel and perpendicular dynamics. In other words, even though β is much larger than in conventional tokamaks, $\widehat{\beta}$ is comparable or only slightly larger as a consequence of the fact that $(L_\parallel/L_\perp)^2$ scales like the square of the aspect ratio.

In general, the electron response in the core is close to adiabatic, with strong correlations between the pressure and the electric potential fluctuations. This implies a loss of a strong source of nonlinearity [4, 5, 35], that is likely to affect the saturated turbulence. From a

modelling point of view, this feature together with the presence of modest gradients paves the way for quasilinear treatments, which have led to successful results.

Finally, it is fair to remark that core turbulence is affected (and sometimes dominated) by effects that are not captured by the fluid parameters that we are using. For example, the physics of the Trapped Electron Modes, which can determine the particle and the electron heat transport is not included in our discussion, as well as the kinetic corrections of the Ion and Electron Temperature Gradient modes (the former responsible for momentum and ion heat transport, the latter contributing to the electron transport). In other words, although the validity of our general arguments still holds in the core, it should be complemented by the analysis of other relevant dimensionless parameters (e.g. the ion/electron temperature ratio, the normalized ion and electron gradient scale lengths, the fraction of trapped particles and so on).

The trend of the dimensionless parameters across the machines are similar in L-mode and in H-mode. However, the absolute values can be orders of magnitude different. This is due to the change in the density and temperature profiles, and in particular to the smaller equilibrium gradients in the boundary of the plasma. Thus, we do not expect significant differences in behaviour of the turbulence in the core, as a consequence of the stiffness of the profiles.

B. Edge

A completely different situation occurs in the edge region, where none of the physical effects associated with the dimensionless parameters can be ignored and hence the electron response is intrinsically non-adiabatic. Between the pedestal top and the separatrix, electromagnetic, inertial and collisional effects are significant in both large and small machines. Moreover, the presence of neutral particles is likewise important in this region, so that ionization (plasma sources) and interaction with other species (collisions with ions and electrons) should in principle be taken into account. Finally, even the assumption that the plasma is magnetized is only marginally correct in the small machines (see Fig.10). All these elements sum up to produce the high degree of dynamical complexity observed in the edge region of the plasma.

The large value of $\widehat{\beta}$ suggests that the turbulence and the plasma instabilities (ELMs)

can have a large magnetic component, which in turn can generate a wide stochastic layer in the vicinity of the axisymmetric separatrix [36]. This leads to a broadening of the separatrix, which is associated with a larger magnetic footprint on the divertor plates. Such a broadening, which grows with the amplitude of the perturbations, could play a role in the recently observed increase of the ELM wetted area as a function of the ELM energy [37]. In this regard, the SXD geometry seems to be beneficial, since our projections for MAST Upgrade show a higher level of electromagnetic fluctuations, which would correspond to a broader divertor footprint.

The ELM size, defined as the ratio between the energy lost at an ELM normalized to the pedestal energy, is experimentally correlated with the pedestal ν_*, and therefore to C [34]. As a consequence, hotter machines such as ITER or DEMO are expected to produce more energetic ELMs, which could potentially damage the divertor and the other Plasma Facing Components.

Because of the more gentle profile gradients, the L-mode edge is less electromagnetic and, despite a colder plasma, the effect of the collisions is less important than in H-mode. Nevertheless, the turbulence is still strongly non-linear and non-adiabatic since $\widehat{\beta}$, $\widehat{\mu}$ and C remain above unity in this region. In the edge, the L-mode cross field heat and particle convection (i.e. the turbulent heat and particle transport) strongly depend on the parameters $\widehat{\beta}$ and C, as extensively discussed in several numerical works [4, 5, 38]. In particular, a combination of large collisionality and large pressure gradients (i.e. large $\widehat{\beta}$) was found to strongly increase the perpendicular transport, suggesting the possibility of a turbulent density limit occurring well before the ideal MHD one, which is triggered by ballooning modes. On the opposite side of the phase parameter space (at low collisionality and large $\widehat{\beta}$) Rogers et al. [39] observed a reversed behaviour, with the transport decreasing with steeper pressure gradients. These numerical studies were substantiated by experimental observations in ALCATOR C-MOD, which confirmed the general trend and therefore the appropriateness of the theoretical models employed [12].

It is interesting to note that in the edge the coupling between the perpendicular dynamics, caused by the drift wave turbulence, and the parallel motion, due to Alfvén wave physics, is mediated by the parameter $\widehat{\beta}$, and is weaker in L-mode than in H-mode. A recent work suggested that, in the core, the presence of a strong coupling between these waves can favour the formation of zonal perturbations and therefore the generation of beneficial velocity shears

which can lead to Internal Transport Barriers [40]. In other words, the coupling allows the energy of the turbulence to efficiently flow into harmless (from a cross field transport point of view) $m = n = 0$ modes. The same mechanism could be at work also in the edge, although its mathematical treatment is much more difficult. If this was the case, the parameter $\widehat{\beta}$, or some elaboration of it, could represent the figure of merit for the formation of the Edge Transport Barrier, and therefore for the L-H transition. Recently, a criterion for the L-H transition which exploits these ideas and which provides a remarkable agreement with the experimental scalings [25] was derived. The results presented in our work are consistent with the theoretical assumption of Ref.[25], in the sense that they show that the L- and H-mode $\widehat{\beta}$ in the edge are indeed different by orders of magnitude.

C. SOL

We first note that both in H- and L-mode the transition across the separatrix is rather smooth and the dimensionless parameters do not change abruptly from the edge to the near SOL. This is an indication of the strong coupling of the two regions.

Analysis of experimental measurements [12] have established a relation between the collisionality parameter, C, and the fraction of power deposited on the divertor. In particular, an increasing C is associated with a larger cross-field transport, which should widen the SOL and direct a greater part of the plasma flux toward the wall instead of the divertor. This picture is consistent with the theoretical models based on Drift-Alfvén dynamics. It is also useful to remark that the SXD configuration would significantly increase C in the SOL of the MAST device, which we expect will lead to an intensification of the wall losses.

In the SOL, the physics of the turbulence is strongly affected by the fact the that magnetic field lines are open and connected to a solid target [41]. The significant difference with respect to the well confined regions can be captured using appropriate boundary conditions for the plasma equations. An important implication of the presence of the solid target is that the double periodicity (poloidal and toroidal) imposed by the field line connection is no longer required. As a consequence, the turbulent inverse energy cascade can access vanishing parallel wave numbers and create elongated convective cells [42]. The turbulence associated with these structures is of interchange nature since the parallel dynamics, responsible for the drift-wave energy distribution, is weakened by the accessibility of $k_{\|} \approx 0$ modes.

D. Divertor

The two point model is a simple, yet powerful and successful, tool to relate the equilibrium density and temperatures in the upstream SOL with those in the divertor region [24]. In particular, this model predicts that the parallel temperature gradients are almost negligible when the collisionality (and therefore C) is moderate, while they become significant when this quantity is increased. Thus, the SOL shifts from the so-called sheath-limited regime, in which the energy transport is mainly convective, to the conduction-limited regime, in which conduction dominates.

The latter is a more desirable regime of operation for the divertor, since it allows high upstream temperatures (i.e. at the last closed field surface) and low target loads. These are obtained as a result of the reduced downstream temperature, which is beneficial by itself and also leads to the formation of a cloud of neutral particles in front of the divertor, thus further shielding it (detached divertor). Figure 4 suggests that in the SOL C is such that large experiments, like ITER and DEMO, should be able to achieve detached operation (crucially, this prediction rests on the accuracy of our estimates of $L_\perp$ in the SOL).

In addition to the complication due to a significant presence of neutrals in front of the detached divertor, the theoretical and numerical modelling of this region is challenging because the ions are weakly magnetised. Indeed, Fig. 11 shows that here ν_i/Ω_i is above unity in all the machines, so that the collisions are so frequent that the ions are not able to complete a single gyro-orbit. As a result, the closure model discussed in Section II loses its validity. Moreover, the perpendicular transport approaches here the level of the parallel transport, since the magnetic field loses its ability to confine the plasma (i.e. isotropy is partially recovered and $\Gamma_\perp \sim \Gamma_\parallel$ and $q_\perp \sim q_\parallel$). An important implication is that detachment models based on multi-fluid codes with constant cross-field transport coefficients underestimate the radial fluxes and hence the degree of detachment. This could be a possible explanation for the inability of the computational approaches to quantitatively reproduce the experimental observations of the detachment dynamics [43, 44].

TABLE VII. Summary of the magnitude of the relevant plasma dimensionless parameters in H-mode. Each cell shows the typical range of the parameter for the profiles investigated. When the cell is dark (light) gray, the physical mechanism associated with the parameter cannot be neglected for all the machines (only for small machines).

		Edge		SOL		Detached
	Core	Pedestal Top	Separatrix	Near SOL	Far SOL	Divertor
$\widehat{\beta}$	$10^{-2} \div 10^{-1}$	$10^{1} \div 10^{2}$	$10^{2} \div 10^{3}$	10^{1}	$10^{-2} \div 10^{-1}$	$10^{-4} \div 10^{-2}$
C	$10^{-6} \div 10^{-5}$	$10^{-2} \div 10^{-1}$	$10^{1} \div 10^{2}$	$10^{1} \div 10^{2}$	$10^{0} \div 10^{1}$	$10^{2} \div 10^{4}$
$\widehat{\mu}$	10^{-3}	$10^{0} \div 10^{1}$	$10^{2} \div 10^{3}$	$10^{2} \div 10^{3}$	$10^{0} \div 10^{1}$	$10^{-2} \div 10^{0}$
D_η/D_{GB}	$10^{-4} \div 10^{-2}$	$10^{-3} \div 10^{0}$	$10^{0} \div 10^{1}$	$10^{2} \div 10^{3}$	$10^{3} \div 10^{4}$	$10^{6} \div 10^{9}$
δ	$10^{-3} \div 10^{-2}$	10^{-2}	$10^{-3} \div 10^{-1}$	$10^{-3} \div 10^{-1}$	$10^{-3} \div 10^{-2}$	$10^{-4} \div 10^{-3}$
ν_i/Ω_i	$10^{-7} \div 10^{-4}$	$10^{-6} \div 10^{-3}$	$10^{-4} \div 10^{-3}$	$10^{-4} \div 10^{-2}$	$10^{-4} \div 10^{-2}$	10^{0}

E. Integration of the regions

The analysis drawn in the previous subsections has emphasized the great variability of the plasma regimes in the different regions of the experimental machines. This obviously makes any attempt to provide a comprehensive description of the plasma challenging. In the last few years, the community has devoted a significant effort toward the development of integrated tools which could provide a complete simulation package for fusion plasma experiments [45] (specifically, ITER and DEMO). From this perspective, it is useful to provide a visual summary of the results discussed in the previous sections.

A few simple conclusions can be drawn from Table VII. Firstly, it suggests a selective use of reduced physical models aimed at the description of the specific regions under investigation, as the available computational resources are not sufficient to resolve the complexity of the whole plasma. Symmetrically, this also implies that theoretical models and numerical codes developed for one region of the plasma (e.g. the core) cannot be straightforwardly applied to another region (e.g. the edge or the SOL), as the response of the electrons is governed by different physical mechanisms. For example, an electrostatic approach with adiabatic electrons is quite common in core turbulence simulations, but would be inappropriate in edge studies. To further complicate things, δ slightly below unity implies that

close to the separatrix even the more consolidated theoretical models lay their foundations on weak grounds (a similar situation occurs close to the detached divertor).

A second conclusion is that the plasma edge (including the near SOL) is by far the most complicated region to model, as a consequence of the fact that several different mechanisms play a significant role in its dynamics. In addition to those summarized in Table VII, it is worth mentioning also the effect of the neutral particles recycled from the wall and the divertor and of the stochastization of the magnetic field due to the non-axisymmetric fluctuations.

V. SUMMARY AND CONCLUSIONS

In this paper we have characterized the turbulence and its associated transport as a function of dimensionless parameters, the most relevant of which represent the strength of the electromagnetic ($\widehat{\beta}$), the collisional (C) and the inertial ($\widehat{\mu}$) effects.

Using experimental L- and H-mode density and temperature profiles, we identified clear trends in the dimensionless parameters in several devices. In particular, we have shown that, despite the difference in engineering parameters, all the machines show a similar behaviour in dimensionless parameters. This can be read as an indication that the turbulence features are well represented by the parameters chosen and that an almost universal behaviour is present. In addition, our analysis shows that the magnitude of the same dimensionless parameter can significantly change from one region to another. This translates into a clear separation between core, edge, SOL and divertor regions, in which different mechanisms dominate the turbulence and can be represented with simplified local models. These mechanisms have been discussed and related to the relevant dimensionless parameters. We interpret the observed universal behaviour as a consequence of a high degree of self-organization in the plasma.

On this basis, dimensionless analysis can also be seen as a tool to increase the confidence in larger machine extrapolations. At the same time, it can be used as guidance and provide physical insight for new conceptual designs, such as the Super-X divertor in MAST-Upgrade. To confirm that, we included in our study future machines such as MAST-Upgrade, ITER and DEMO. It is interesting to note that the dimensional parameters obtained from the theoretical and numerical predictions available in literature for these future experiments are

indeed consistent with the trends observed for present experimental devices.

In conclusion, the observed clustering of the dimensionless parameters reinforces the notion that present-day machines can be used for similarity experiments and can thus produce meaningful extrapolations for ITER and DEMO. On the other hand, the robustness of a code or a theory can be certified only if it is able to properly represent the dynamics of the plasma in several devices. Indeed, the presence of weaker sub-dominant trends within the universal structure introduces non-trivial machine dependencies. The ability to capture this behaviour determines a strong requirement for the numerical or analytical models, the reliability of which (and indirectly, the capability of giving good extrapolations) can be therefore assessed only through a multi-machine validation process.

In addition, different physical mechanisms dominate different regions of the plasma. The separation between core, edge, SOL and divertor is a useful expedient which allows a simplified treatment of the dynamics, compatible with the numerical constraints. It is therefore natural to construct *ad hoc* models which capture the locally relevant physics and neglect the rest. Despite its usefulness, this reductionist approach has its drawbacks. Indeed, in order to provide a global account of the behaviour of the plasma, the different local models need to be integrated over the plasma regions discussed above and the correctness of this procedure seems to be a key element to properly describe the dynamics. This task, complicated by the complexity of the physics and the limitations of the computational resources, is probably essential in order to shed some light over some of the most crucial and elusive plasma phenomena, such as the L-H transition or the density limit.

VI. ACKNOWLEDGEMENTS

FM acknowledges useful discussions with Dr. J. Connor, Dr. V. Naulin and Dr. M. Romanelli. This work was funded by the RCUK Energy Programme under grant EP/I501045 and the European Communities under the contract of Association between EURATOM and CCFE. The views and opinions expressed herein do not necessarily reflect those of the European Commission.

Appendix A: Derivation of Ohm's law in a drift-fluid model

The normalization of the equations is chosen in such a way that it is representative of the phenomena described in Section II A. In particular, the perpendicular and parallel coordinates are normalized to ρ_s and $L_\parallel$ respectively, so that $\overline{\nabla}_\perp = \rho_s^{-1}\widehat{\nabla}_\perp$ and $\overline{\nabla}_\parallel = L_\parallel^{-1}\widehat{\nabla}_\parallel$ and the time scale is set by the perpendicular transit time: $\partial/\partial\overline{t} = (c_s/L_\perp)\partial/\partial\widehat{t}$. Here, we use the over-line symbol for the dimensional quantities and the hat symbol for the normalized ones. We define the parallel and perpendicular gradients as $\nabla_\parallel = \mathbf{B}/B\cdot\nabla$ and $\nabla_\perp = \nabla - \nabla_\parallel$. We are specifically interested in the evolution of the perturbation of the equilibrium, which are assumed to be a factor δ smaller than their equilibrium counterpart (i.e. we have small fluctuations). As a consequence, all the field variables (temperature, density, velocity, current *et cetera*) can be split into an equilibrium and a fluctuating part. The former is normalized by its characteristic local value, while the latter by the same factor times δ. In particular, for the plasma density, electron temperature and pressure, we have: $\overline{n}_{tot} = n_0(\widehat{n}_{eq} + \delta\widehat{n})$, $\overline{T}_{e,tot} = T_{e0}(\widehat{T}_{e,eq} + \delta\widehat{T}_e)$, $\overline{p}_{e,tot} = n_0 T_{e0}(\widehat{p}_{e,eq} + \delta\widehat{p}_e)$ while the amplitude of the equilibrium magnetic field is given by $\overline{B} = B_0\widehat{B}$. We also assume that the equilibrium quantities vary on a much longer scale than the fluctuations, so that $\overline{\nabla}_\perp\widehat{f}_{eq} = L_\perp^{-1}\widehat{\nabla}_\perp\widehat{f}_{eq}$ and similarly, $\overline{\nabla}_\parallel\widehat{f}_{eq} = \delta\widehat{\nabla}_\parallel\widehat{f}_{eq}$ where $\widehat{f}_{eq}$ is a generic normalized equilibrium function (note that the parallel gradient of an equilibrium function is different from zero only because of the electromagnetic perturbations which modify the operator).

The perpendicular electric field is assumed to be relatively small in the drift-ordering, so that the $\mathbf{E}\times\mathbf{B}$ velocity is comparable with the diamagnetic velocity and both scale like δc_s. As a consequence, we have that $\overline{\mathbf{V}}_E \equiv -c\overline{\mathbf{B}}\times\overline{\mathbf{E}}/B_0^2 = \delta c_s\widehat{\mathbf{V}}_E$.

The parallel electric field perturbation, which is free from the drift ordering constraint, is given by $\overline{E}_\parallel = \delta[T_{e0}/(eL_\parallel)]\widehat{E}_\parallel$. The dimensionless electric potential becomes $\overline{\phi}_{tot} = (T_{e0}/e)(\widehat{\phi}_{eq} + \delta\widehat{\phi})$, which implies that the electric energy of the perturbations is order δ with respect to the internal energy of the plasma.

Despite the difference in the magnitude of their equilibrium parts, the perturbed components of the parallel ion and electron velocities, $\overline{V}_{\parallel i,e}$ are normalized with respect to the same quantity, $\delta c_s L_\parallel/L_\perp$, in agreement with the procedure used in Ref.[4]. With this convention, the dimensionless parallel velocity is much smaller for the ions than for the electrons (the latter is of order unity if we assume that $\sqrt{m_e/m_i} \sim L_\perp/L_\parallel$). As a consequence of their

fast motion in the direction of the magnetic field, the parallel current is mostly driven by the electrons. This is taken into account when we express the dimensionless current, so that $\overline{J}_\parallel = (en_0c_sL_\parallel/L_\perp)(\widehat{J}_{\parallel,eq} + \delta\widehat{J}_\parallel)$. Finally, the perturbed parallel vector potential, $\overline{A}_\parallel$, is normalized with respect to $\delta B_0\rho_s\beta L_\parallel/L_\perp$ where $\beta = 4\pi n_0 T_{e0}/B_0^2$.

For the sake of simplicity, from now on and in the main text we drop the hat symbol, so that all the variables in the equations refer to perturbations unless otherwise specified.

With this convention, the parallel part of the dimensionless Faraday's law is:

$$E_\parallel = -\nabla_\parallel\Phi - \widehat{\beta}\frac{\partial A_\parallel}{\partial t}, \tag{A1}$$

where $\Phi = \phi + \phi_{eq}$. The parameter $\widehat{\beta} \equiv \beta(L_\parallel/L_\perp)^2$ determines the importance of the electromagnetic contribution to the electric field and is the first of the dimensionless parameters that we consider.

The dynamics of the electrons are described by the generalized Ohm's law, Eq.1, which is obtained by projecting the electron momentum conservation equation along the magnetic field direction. Using the diamagnetic cancellation [8], assuming the magnetic field to be dominated by its toroidal component, neglecting the electron viscosity, which is proportional to the electron mass and drop the density perturbations, we obtain:

$$\widehat{\mu}\left(\frac{\partial}{\partial t} + \mathbf{V}_E\cdot\nabla\right)V_{\parallel,e} = -\nabla_\parallel(p_e + p_{e,eq}) - E_\parallel + F_\parallel - \widehat{\mu}(\mathbf{V}_{E,eq}\cdot\nabla V_\parallel + \mathbf{V}_E\cdot\nabla V_{\parallel,eq}), \tag{A2}$$

where $\widehat{\mu} \equiv (m_e/m_i)\epsilon_s$ and $F_\parallel$ is the parallel component of the friction force. For the latter we use Braginskii's expression: $F_\parallel = CJ_\parallel - 0.71\nabla_\parallel(T_e + T_{e,eq})$ with $C \equiv 0.51\widehat{\mu}\nu_e/(c_s/L_\perp)$. Despite the fact that in the previous expression for $F_\parallel$ the term representing the thermal force is formally independent from the collision frequency, it does vanish in absence of collisions (i.e. for $C \to 0$). Indeed, its derivation is strictly rigorous only within the collisional regime, $c_s/L_\perp \ll \nu_e \ll \Omega_e$, and its functional dependence would therefore need to be modified in the collisionless case, $\nu_e \ll c_s/L_\perp$. As a consequence, some authors prefer to express the thermal force as a function of the parallel current and heat flux [4] and provide an equation for the latter, while others use so called 'Knudsen corrections' [9] which limit the parallel conductivity with *ad hoc* models. Using Eqs.A1 we obtain form Eq.A2:

$$\widehat{\beta}\frac{\partial A_\parallel}{\partial t} + \widehat{\mu}\left(\frac{\partial}{\partial t} + \mathbf{V}_E\cdot\nabla\right)J_\parallel = \nabla_\parallel(p_e - \phi) - CJ_\parallel + 0.71\nabla_\parallel T_e + S_{eq}^{(4)}, \tag{A3}$$

where $S_{eq}^{(4)} = -\widehat{\mu}(\mathbf{V}_{E,eq}\cdot\nabla J_\parallel + \mathbf{V}_E\cdot\nabla J_{\parallel,eq}) + \nabla_\parallel(p_{e,eq} - \phi_{eq}) + 0.71\nabla_\parallel T_{e,eq}$. We have also replaced $V_{\parallel,e}$ with $J_\parallel$ as their difference only introduces a small correction to the parallel

pressure gradient (as obtained from the parallel ion momentum conservation). Equation A3 plays a central role in the definition of the nature of the turbulence because it describes the dominant physical effects that control the parallel electron response and the deviations from the adiabatic state. This, in turn, determines the strength and features of the nonliearities which affect the transport. Three dimensionless parameters that appear in Ohm's law, $\widehat{\mu}$, $\widehat{\beta}$ and C. The first of these weighs the contribution of the electron inertia and introduces time delays in the response of $J_{\parallel}$. The parameter $\widehat{\beta}$ represents the strength of the magnetic induction and determines the importance of the electromagnetic effects on the electron dynamics. Finally, C measures the magnitude of the collisional terms (including the thermal force). In absence of all these effects, the electron response is perfectly adiabatic with pressure and electric potential fluctuations strongly tied with each other (which implies a weakening of the nonlinear effects).

Appendix B: Typical profiles and variability

In order to characterise a *typical* pulse in L- or H-mode in the machines that we examined, we used two approaches. The first consists in doing a statistical analysis of the ITPA databases, which contains an extensive collection of data on the density and temperature profiles. This allowed us to rigorously calculate average values and to estimate how large is the variability of the plasma conditions from pulse to pulse. However, these data are limited to the active machines and they do not include the region beyond the separatrix. As a consequence, all the values for ITER, DEMO and MAST SXD and those in the SOL for the remaining machines had to be determined in a different way. For the future machines, this gap was filled using published theoretical and numerical predictions or extrapolations from active devices. The SOL data were extracted from publications that reported experimental measurements (the number of which was not sufficiently large to justify a statistical analysis). The variability of these data was estimated using theoretical considerations (e.g. based on the two point model for C) or extrapolating from core results ($\widehat{\beta}$ and $\widehat{\mu}$).

To clarify the methodology used in our first approach, we apply it here in detail to JET (for the other machines we only give the final result of the analysis). Using the H-mode and pedestal ITPA databases, we obtain the core and pedestal temperature and density for 162 H-mode pulses (those with small ELMs) and 35 L-mode pulses. At the separatrix the

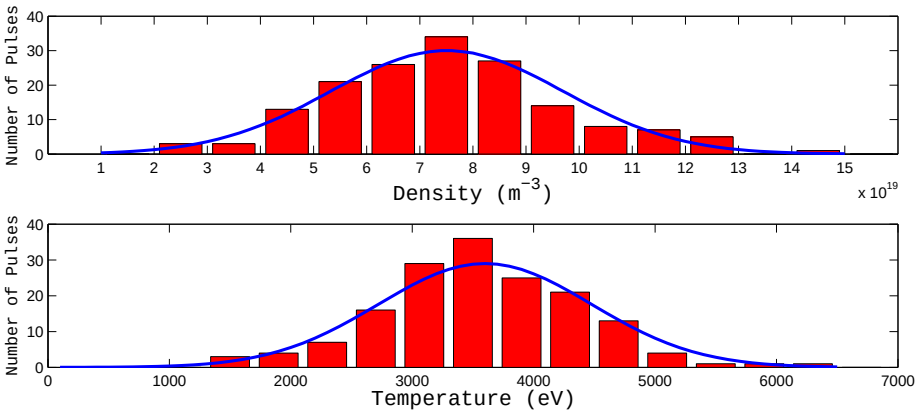

FIG. 12. Statistical distribution of the density and temperature in the core of JET for pulses in H-mode. The solid lines are the normal distributions that best fit the data.

temperature, T_s, was estimated by assuming a conduction limited regime for the SOL [24]. In this case, we have that $T_s \approx [7P_{SOL}/(4\kappa_0 A_\parallel)]^{2/7}$ where P_{SOL} is the power crossing the separatrix, calculated as the total heating power minus the radiated power, $A_\parallel \equiv \lambda_q S_\perp / L_\parallel$ with $S_\perp = 4\pi^2 R^2 \epsilon \kappa^{1/2}$ is the plasma surface at the separatrix (ϵ is the inverse aspect ratio and κ is the elongation) and λ_q is the power e-folding length, estimated as 1% of the minor radius, and finally $\kappa_0 \approx 2000$ [24] is the temperature independent part of the heat conductivity (all the variables are measured in SI, apart from the temperature, for which we use electronVolts). Analogously, for the density we use the scaling formula obtained from a multi-machine study described in [46]: $n_s \approx 0.00236 < n >^{1.08} \kappa^{1.11} B_T^{0.78}$, where $< n >$ is the line averaged density and B_T is the toroidal field (this expression is strictly valid for L-mode, but is used here also for H-mode).

The statistical distributions of the temperature and density in the H-mode JET pulses, shown in Figs.12-14, are well approximated by normal distributions (solid lines in the figures). It is therefore reasonable to define the *typical* value as the mean of the distribution and the variability as the ratio between the standard deviation and the mean (expressed in percentage). The same approach was used for ALCATOR C-MOD, ASDEX-U and MAST (for the latter, only H-mode data were available in the ITPA database). The mean values of the temperature and of the density are collected in the tables in the main text (tables II-V), while the variabilities calculated with the statistical approach are summarized in Tables VIII-IX.

The next intermediate step is to calculate from the same database the mean and the

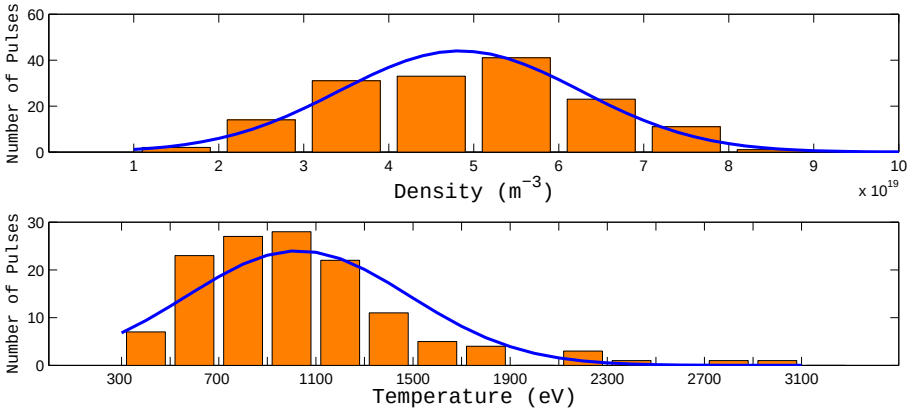

FIG. 13. Statistical distribution of the density and temperature at the pedestal top of JET for pulses in H-mode. The solid lines are the normal distributions that best fit the data.

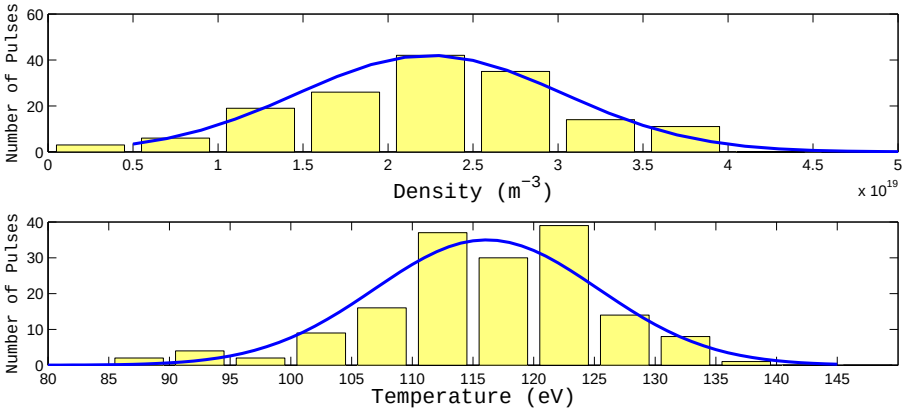

FIG. 14. Statistical distribution of the density and temperature at the separatrix of JET for pulses in H-mode. The solid lines are the normal distributions that best fit the data.

TABLE VIII. H-mode (L-mode in brackets) variability of the plasma density in the regions of the machines where the statistical analysis was possible. The variability is given by the fraction (expressed in %) between the mean value and the standard deviation of the data.

		Edge	
	Core	Pedestal Top	Separatrix
ALCATOR C-MOD	13 (37)	12	15 (32)
ASDEX U.	25 (16)	44	31 (20)
JET	29 (25)	29	34 (30)
MAST	13	12	18

TABLE IX. H-mode (L-mode in brackets) variability of the plasma temperature in the regions of the machines where the statistical analysis was possible. The variability is given by the fraction (expressed in %) between the mean value and the standard deviation of the data.

		Edge	
	Core	Pedestal Top	Separatrix
ALCATOR C-MOD	17 (31)	21	7 (10)
ASDEX U.	35 (15)	40	14 (10)
JET	24 (34)	44	8 (13)
MAST	21	10	8

standard deviation of the Kadomtsev's dimensionless parameters, which are related to ours through Eqs.2-4. We find that the variability of these quantities is again moderate. In particular, according to the database used, β's variability is the largest in ASDEX-U, where it reaches 50% in the pedestal region, while it is smaller in MAST, where it is around 10%. All the other machines have intermediate values between these two. Due to the limited amount of SOL data (extracted from selected works, not from the ITPA databases), we cannot rigorously evaluate the variability of β beyond the separatrix. As a working hypothesis, we assume that it is similar to the core's. From the statistical analysis of the ITPA databases, we find that in the core ρ_* (equal to ρ_s divided by the minor radius) has a maximum variability (around 30%) in JET and a minimum (around 7%) in MAST. Finally, the plasma collisionality can change quite a lot from pulse to pulse. Indeed, its variability can reach 100% (with maximum observed values of 130%), which implies that this parameter can sometimes span more than one order of magnitude (but never more than two for the data analysed). On the other hand, the average value of the collisionality shows a clear machine size dependence (due to better confinement and higher temperature in larger devices) and it can therefore significantly change from machine to machine. For example, in the pedestal region of JET $\nu_* \approx 0.2$, while in the same location of MAST we find $\nu_* \approx 3.5$. This implies that inside the separatrix the machine variability is comparable to the machine to machine variation already taken into account in our discussion. To complete the discussion, experimental observations of JET and ALCATOR C-MOD, interpreted with the two point model by Erents *et al.* [47] suggest that in the conduction limited regime (in

which tokamaks operate frequently) the SOL collisionality lies in a relatively narrow band: $10 \lesssim \nu_* \lesssim 85$.

Finally, the statistical variability of the drift-fluid dimensionless parameters is similar to the variability of the Kadomtsev's parameters as they are related through the factor $L_\parallel/L_\perp$. This factor roughly scales as q/ϵ, which implies that its change is limited by the stability constraints of the plasma. If only baseline scenario configurations are considered, the central safety factor is slightly above unity and from the ITPA databases we find $q_{95} = 3.35 \pm 0.4$ for JET, $q_{95} = 3.9 \pm 0.6$ for ASDEX-U, $q_{95} = 4 \pm 0.5$ for ALCATOR C-MOD and $q_{95} = 5.45 \pm 0.7$ for MAST, which consistently shows a variability around 10-15% (extended also to the other regions of the plasma). From these considerations, we also expect a similar variability for $\widehat{\mu}$, which depends only on $(L_\parallel/L_\perp)^2$. Even including the uncertainties on the calculation of $(L_\parallel/L_\perp)$, the variability of $\widehat{\beta}$ is well below 100% in all the regions of the plasma and in all the machines investigated. Finally, C is the parameter with the largest variability, although still comparable to the spread between the machines. In the SOL, the condition of the collisionality implies that C should range between $5.1\mu^{1/2}$ and $43.35\mu^{1/2}$ (see Eqs.3 and 4). The SOL values for C shown in Fig.4 are compatible with the above discussion as they lie within the theoretical interval.

---

[1] T.C. Luce, C.C. Petty and J.G. Cordey, Plasma Phys. Control. Fusion, 50, 043001 (2008).

[2] B.B. Kadomtsev, Sov. Phys. - J. Plasma Phys., 1, 295 (1975).

[3] J.W. Connor and J.B. Taylor, Nucl. Fusion, 17, 1047 (1977).

[4] B. Scott, Plasma Phys Control. Fusion, 39, 1635 (1997).

[5] B.N. Rogers and J.F. Drake, Phys. Rev. Lett., 79, 229 (1997).

[6] S.I. Braginskii, Rev. Plasma Phys., 1, 205 (1965).

[7] P. Helander and D.J. Sigmar, *Collisional Transport in Magnetized Plasmas*, 2002 (Cambridge: Cambridge University Press).

[8] R.D. Hazeltine and J.D. Meiss, *Plasma Confinement*, 1992 (Redwood City: Addison-Wesley).

[9] A. Thyagaraja, F.A. Haas and I. Cook, Nucl. Fusion, 20, 611 (1980).

[10] S.J. Zweben, J.A. Boedo, O. Grulke, Plasma Phys. Control. Fusion, 49, S1 (2007)

[11] E. Marmar, A. Bader, M. Bakhtiari *et al.*, Nucl. Fusion, 49, 104014 (2009).

[12] B. LaBombard, J.W. Hughes, D. Mossessian *et al.*, Nucl. Fusion, 45, 16581675 (2005).

[13] A. R. Field, R. J. Akers, C. Brickley *et al.*, 'Core Heat Transport in the MAST Spherical Tokamak', 20th IAEA Fusion Energy Conference, Vilamoura, Portugal, 2004, EX/P2-11

[14] V. Rozhansky, E. Kaveeva, P. Molchanov *et al.*, Nucl. Fusion, 49, 025007 (2009).

[15] A. Kirk, G.F. Counsell, W. Fundamenski *et al.*, Plasma Phys. Control. Fusion, 46, 1591 (2004).

[16] J. Neuhauser, D. Coster, H.U. Fahrbach *et al.*, Plasma Phys. Control. Fusion, 44, 855869 (2002)

[17] L.D. Horton, A.V. Chankin, Y.P. Chen *et al.*, Nucl. Fusion, 45, 856 (2005).

[18] B. Kurzan, L.D. Horton, H. Murmann *et al.*, Plasma Phys. Control. Fusion, 49, 825844 (2007).

[19] W. Fundamenski, O.E. Garcia, V. Naulin *et al.*, Nucl. Fusion, 47, 417 (2007).

[20] D. Moulton *et al.*, J. Nucl. Mater. (2011), doi:10.1016/j.jnucmat.2011.02.025

[21] E.J. Doyle, W.A. Houlberg, Y. Kamada *et al.*, Nucl. Fusion, 47, S18 (2007).

[22] C.M Roach, M. Walters, R.V. Bundy *et al.*, Nucl. Fusion, 48, 125001 (2008).

[23] A.Loarte, B. Lipschultz, A.S. Kukushkin *et al.*, Nucl. Fusion, 47, S203 (2007).

[24] P.C. Stangby, *The Plasma Boundary of Magnetic Fusion Devices*, 2002 (Bristol: IOP).

[25] W. Fundamenski, F. Militello, D. Moulton, D.C. McDonald, to be submitted to Nuclear Fusion.

[26] M. Greenwald, R.L. Boivin, F. Bombarda *et al.*, Nuclear Fusion, 37, 739 (1997)

[27] K. Lackner, Comment. Plasma Phys. Control. Fusion, 15, 359 (1994).

[28] M. Romanelli, F. Romanelli, F. Zonca, 'On the Optimal Choice of the Dimensionless Parameters of Burning Plasma Physics Experiments', 43rd Annual Meeting of the APS Division of Plasma Physics, Long Beach, California, 2001.

[29] B. Lipschultz, X. Bonnin, G. Counsell *et al.*, Nucl. Fusion, 47, 1189 (2007).

[30] Y.R. Martin, T. Takizuka and ITPA CDBM H-mode Threshold Database Working Group, Journal of Physics: Conference Series, 123, 012033 (2008).

[31] M. Greenwald, Plasma Phys. Control. Fusion, 44, R27 (2002).

[32] F. Pegoraro, F. Porcelli, T.J. Schepp, Phys. Fluids B, 1, 364, (1989).

[33] F. Porcelli, Phys. Rev. Lett, 66, 425 (1991).

[34] A. Loarte *et al.*, Plasma Phys. Control. Fusion, 45, 1549 (2003).

[35] B.D. Scott, Phys. Rev. Lett., 65, 3289 (1990).

[36] A. Punjabi, A. Verma and A. Boozer, Phys. Rev. Lett., 69, 3322 (1992).

[37] M.W. Jakublowski, T.E. Evans, M.E. Fenstermacher, *et al.*, Nucl. Fusion, 49, 095013 (2009).

[38] V. Naulin, Phys. Plasmas, 10, 4016 (2003).

[39] B.N. Rogers, J.F. Drake and A. Zeiler, Phys. Rev. Lett., 81, 4396 (1998).

[40] F. Militello, M. Romanelli, J.W. Connor, R.J. Hastie, Nucl. Fusion, 51, 033006 (2011).

[41] W. Fundamenski, *Power Exhaust in Fusion Plasmas*, 2009 (Cambridge: Cambridge University Press).

[42] T.T. Ribeiro and B. Scott, Plasma Phys. Control. Fusion, 47, 1657 (2005).

[43] M. Wischmeier and M. Groth and A. Kallenbach *et al.*, J. Nucl. Mater., 390, 250 (2009).

[44] V. Kotov and D. Reiter, Plasma Phys. Control. Fusion, 51, 115002 (2009).

[45] A. Bécoulet,P. Strand, H. Wilson, M. Romanelli, L.-G. Eriksson, Comput. Phys. Comm., 177, 55 (2007).

[46] G.D. Porter, S. Davies, B. LaBombard *et al.*, J. Nucl. Mater., 917, 226 (2010)

[47] S.K. Erents, P.C. Stangeby, B. LaBombard, J.D. Elder and W. Fundamenski, Nucl. Fusion, 40, 295 (2000)